

## Design and Optimization of Conforming Lattice Structures

Wu, Jun; Wang, Weiming; Gao, Xifeng

**DOI**

[10.1109/TVCG.2019.2938946](https://doi.org/10.1109/TVCG.2019.2938946)

**Publication date**

2021

**Document Version**

Accepted author manuscript

**Published in**

IEEE Transactions on Visualization and Computer Graphics

**Citation (APA)**

Wu, J., Wang, W., & Gao, X. (2021). Design and Optimization of Conforming Lattice Structures. *IEEE Transactions on Visualization and Computer Graphics*, 27(1), 43-56. Article 8823060.  
<https://doi.org/10.1109/TVCG.2019.2938946>

**Important note**

To cite this publication, please use the final published version (if applicable).  
Please check the document version above.

**Copyright**

Other than for strictly personal use, it is not permitted to download, forward or distribute the text or part of it, without the consent of the author(s) and/or copyright holder(s), unless the work is under an open content license such as Creative Commons.

**Takedown policy**

Please contact us and provide details if you believe this document breaches copyrights.  
We will remove access to the work immediately and investigate your claim.

# Design and Optimization of Conforming Lattice Structures

Jun Wu, Weiming Wang, Xifeng Gao

**Abstract**—Inspired by natural cellular materials such as trabecular bone, lattice structures have been developed as a new type of lightweight material. In this paper we present a novel method to design lattice structures that conform with both the principal stress directions and the boundary of the optimized shape. Our method consists of two major steps: the first optimizes concurrently the shape (including its topology) and the distribution of orthotropic lattice materials inside the shape to maximize stiffness under application-specific external loads; the second takes the optimized configuration (i.e. locally-defined orientation, porosity, and anisotropy) of lattice materials from the previous step, and extracts a globally consistent lattice structure by field-aligned parameterization. Our approach is robust and works for both 2D planar and 3D volumetric domains. Numerical results and physical verifications demonstrate remarkable structural properties of conforming lattice structures generated by our method.

**Index Terms**—Lattice structures, topology optimization, homogenization, 3D printing.



## 1 INTRODUCTION

The design of lightweight structures by optimization is a classical and still active topic in engineering. Stimulated by the increasingly high flexibility and resolution offered by 3D printing, there has been a growing interest in optimizing structures that are composed of delicate microstructures [1], [2]. These approaches assume that the microstructures are aligned with a prescribed regular grid. This simplifies modelling, simulation and optimization. It, however, limits the solution space, and thus the achievable structural performance. The microstructures are typically anisotropic (e.g. a hollowed cubic cell with uniform thickness is stiffer along its axes than along its diagonals). It is known that the orientation of anisotropic materials in stiffness-optimal structure coincides with the principal stress directions resulting from forces acting on these materials [3]. Furthermore, axis-aligned microstructures do not match the curved surfaces of 3D shapes, which may create problems in assembly of mechanical components.

To address the above issues, in this paper we propose an efficient and robust method to generate *conforming* lattice structures. A *lattice* is a connected array of struts. The lattice structure generated by our method is conforming in two aspects: the struts align with principal stress directions, maximizing structural stiffness; and, struts on the boundary capture the curved surface of the optimized shape. We note

that the shape, according to design options accessible to the user, is allowed to evolve together with the optimization of lattice distribution, i.e. the optimized shape is a subset of the design domain.

Our method has two major steps, in line with the homogenization-based optimization method proposed by Bendsøe and Kikuchi [4] and the post-treatment of the homogenization proposed by Pantz and Trabelsi [5] which was recently revisited [6], [7]. In the first step of our method, both the shape and the spatially-varying orientation of lattices inside the shape evolve simultaneously according to stress analysis and numerical optimization. Rather than relying on extremely high-resolution finite elements to capture the evolving lattice geometric details, we develop a homogenization-based topology optimization method which allows to efficiently simulate and optimize the lattice material distribution on a relatively coarse level. By introducing a novel parameterization of the unit cell, our method ensures a uniform thickness of struts while allowing a sufficient degree of lattice anisotropy. The second step, which we call *lattice compilation*, extracts a globally consistent lattice structure from the optimized, locally-defined lattice configuration, including orientation, porosity, and anisotropy. We address the challenging problem of extracting connected lattices across cells with spatially-varying orientation, by extending field-aligned meshing techniques. This extension allows a fast and robust lattice compilation where anisotropic geometric features are incorporated.

The specific contributions of our paper include:

- Jun Wu and Weiming Wang are with the Department of Design Engineering, Delft University of Technology, Delft, The Netherlands.
- Xifeng Gao is with the Department of Computer Science, Florida State University, US.
- Weiming Wang is also with the School of Mathematical Sciences, Dalian University of Technology, China.
- Corresponding Author: Jun Wu, E-mail: j.wu-1@tudelft.nl

- A novel workflow for designing, in both 2D and 3D, conforming lattice structures based on homogenization-based topology optimization and field-aligned parameterization.
- A simple and effective parameterization of the unit cell for allowing structural anisotropy while ensuring a uniform thickness of struts.

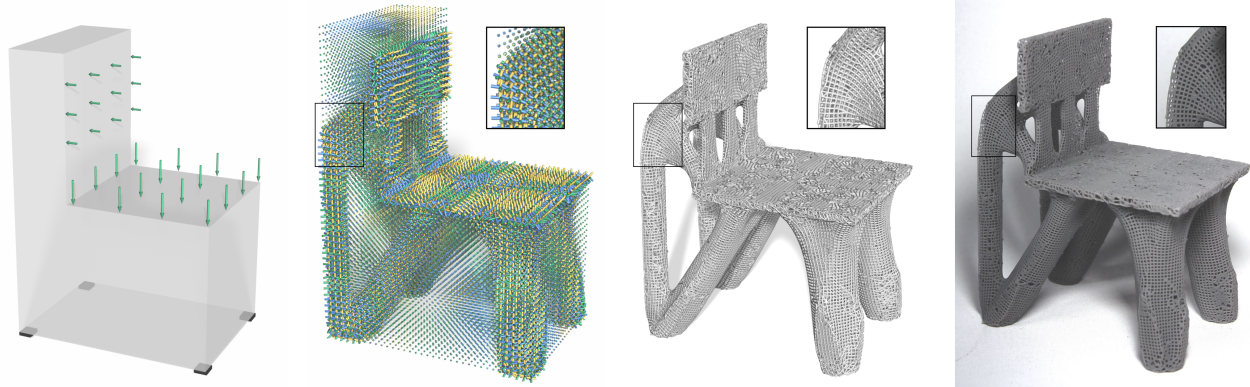


Fig. 1: From left to right: Given a design domain with specified external loads, our method optimizes the distribution of lattice materials for maximizing stiffness. From the optimized, locally-defined lattice configuration, a globally connected lattice structure is compiled, and fabricated by 3D printing.

- A new formulation to allow simultaneous optimization of the shape and the lattice distribution.
- A novel approach for extracting globally consistent lattice structures that accommodate anisotropy and heterogeneity.

Our method generates highly detailed lattice structures. The optimized lattice chair in Figure 1, for instance, consists of 178,291 struts, achieved on a simulation resolution of  $140 \times 100 \times 200$ .

The remainder of the paper is organized as follows. In the next section we review related work. In Section 3 we give an overview of the proposed method. In Sections 4 and 5 the two major steps of our method, lattice optimization and compilation, are presented. Results and analysis are presented in Section 6, before the conclusions are given in Section 7.

## 2 RELATED WORK

### 2.1 Structural Optimization for 3D Printing

In the era of 3D printing (and more broadly, digital fabrication), structural optimization becomes increasingly relevant in computational design [8]. Skin-frame structures [9], honeycomb-like Voronoi structures [10], tree-like supporting structures [11], and bone-inspired porous structures [12] have been optimized as lightweight infill for prescribed 3D shapes. Guided by outputs from structural optimization, Martinez et al. proposed to use graded orthotropic foams as a parameterized metamaterial to fill a prescribed shape [13], [14]. In contrast to design and optimize internal structures for prescribed shapes, our method optimizes concurrently the shape and its internal microstructures for application-specific loads. Different from two-scale structural optimizations (e.g. [15], [1]) which assume axis-aligned microstructures, our method optimizes the orientation of microstructures, in particular, to align it with spatially-varying stress directions. We restrict our design method to lightweight microstructures that are composed of struts, i.e. lattice structures. We note that lattice structures are less optimal than closed-walled shell structures regarding stiffness, yet they have potential benefits regarding, among others, structural stability and manufacturing [16].

Lattice structures are typically aligned with a regular grid [17], [18]. Rosen and his co-authors proposed a method

to design lattice structures that conform with the boundary surface of a prescribed 3D shape [19], [20]. Our method optimizes concurrently the shape and align the lattices with stress directions. The alignment of structures along principal stress directions improves structural performance [21], [3]. This principle has been applied to 2D planes (e.g. [22]) and curved surfaces [23], [24], [25]. The appealing 2D results are achieved by tracing stress directions or based on a ground structure approach [26], [27]. Due to their inherent challenges associated with the initialization of samples/nodes, a direct extension of these methods to 3D volumetric lattices is not applicable. Our method constructs stress-aligned 3D volumetric lattices, relying on homogenization-based topology optimization and field-aligned meshing.

Our method is among recent efforts on structural analysis and optimization for 3D printing. Stava et al. proposed a method to detect and correct structural defects [28]. Recent efforts include worst-case structural analysis [29], [30], and stochastic structural analysis [31]. Chen et al. proposed a solver for inverse elastic shape design [32]. Ulu et al. optimized structures under force location uncertainty [33]. Our method, targeting on stiffness maximization of lattice structures under certain static loads, is complementary to these efforts. Yet the integration goes beyond the scope of this paper.

### 2.2 Homogenization-based Topology Optimization

Topology optimization is an important design method for 3D printing, as it effectively leverages the fabrication flexibility to create structures with exceptional (mechanical) properties. Topology optimization transforms optimal shape design as a material distribution problem. In their seminal work, Bendsøe and Kikuchi proposed a homogenization method, which optimizes the distribution of square unit cells with variable rectangular holes [4]. Due to the lack of manufacturing means for such microstructures back then, the homogenization method was replaced by density-based approaches (e.g. SIMP [34]) which have since been widely used in industry and in many academic contributions (e.g. large scale optimization [35], [36], [37]).

In light of the capability of 3D printing to fabricate microstructures, the homogenization method was recently revisited to design structures with manufacturable mi-

crostructures [6], [7], [38], based on the rectangular hole model [4]. A challenge is to compile a continuous structure from hollowed cells that are defined on a regular grid, and that, after optimization, have different orientations. To this end, a projection approach proposed by Pantz and Trabelsi [5] was improved to connect the orthotropic microstructures [6], [39]. The output structure is represented by high-resolution pixels or voxels.

Our approach to design conforming lattice structures follows the homogenization approaches, but differs in three aspects. First, we propose a new parameterization of cells to ensure that the variable cells have a constant thickness, while allowing a large degree in anisotropy. Our intention of creating uniform thickness is to simplify all downstream operations including surface mesh creation, process planning, fabrication, surface treatment, inspection and qualification. Uniform thickness is a common practice in (metal) additive manufacturing of (axis-aligned) lattices [17], [18]. Such structures can also be fabricated by a direct extrusion in 3D [40], or by robotic fabrication [41], [42]. We note that variable thickness is not impossible with 3D printing. Second, our method simultaneously optimizes the lattice distribution and the shape, achieved using multiple design variables. Last but not least, while existing works exploited projection methods for generating high-resolution pixel or voxel models, we develop a novel approach based on field-aligned meshing to compile the lattice structure. The optimized structure is compactly represented by a graph. This direction shares a similar goal with the recent work by Arora *et al.* [43]. In contrast to the design approach [43], our method unlocks a large solution space by optimizing the porosity, anisotropy, and orientation of lattices.

### 2.3 Field-aligned Parameterization

We develop a lattice compilation method based on field-aligned parameterization which has been researched intensively in the past decade, especially for generating quadrilateral (quad-) mesh. We review briefly the more recent works on hexahedral (hex-) meshing, and for quad-meshing we refer an interested reader to the survey by Bommers *et al.* [44].

For a given 3D closed shape, field-aligned hex/hex-dominant meshing techniques typically consist of three steps [45], [46], [47], [48], [49], [50]. It starts by estimating the gradients of a volumetric parameterization using a directional field [51], [52], where the field is discretized per vertex or per tetrahedron and smoothly interpolated within the volume under a boundary alignment constraint. This is followed by computing a parameterization aligned with the estimated gradients by fitting. Finally it extracts the hex-mesh in the parametric space [53]. Robust hex-meshing remains a challenging problem. A promising direction is to topologically correct the directional fields [47], [48], [54], [55]. Lei *et al.* introduced a hex-mesh generation method based on surface foliation theory [56]. This approach, however, requires heavy topological pre-processing of the input.

The field-aligned parameterization pipeline is primarily used for generating semi-regular meshes. To ensure the validity of the mesh, complex geometric and topological computations are involved. In this paper we make use of

field-aligned parameterization to generate lattice structures. This new application differs from mesh generation, as lattices are encoded by graphs rather than meshes. This goal sidesteps the numerical stability issue and geometrical and topological complexities typically occurred during mesh extraction from the parameterization.

To efficiently and robustly extract consistent lattice structures, we extend the robust meshing approach that was proposed by Jacob *et al.* [57] and further developed by Gao *et al.* [50]. The per vertex local parameterization from [50] fits our purpose well since the local parameterization aligns exactly with the direction field by construction and permits fast and scalable computations. The extension proposed in this paper allows to incorporate anisotropy and heterogeneity.

The recent work by Arora *et al.* [43] shares a similar goal as ours, *i.e.* to extract field aligned struts from stress directions. Our approach takes the optimized stress fields as input, without a field smoothing operation that compromises the accuracy of input fields. During lattice compilation, while they extract the struts by tracing stress lines and simplifying the duplicated ones, our approach directly generates struts by simple and efficient graph operations. This makes our approach fast and scalable, taking a couple of minutes for an input with tens of millions of tetrahedral elements (see Table 2).

## 3 OVERVIEW

Given a design domain and application-specific loads, our method generates a lattice structure that maximizes structural stiffness. The struts in the optimized lattice structure conform with principal stress directions. Moreover, the struts on the boundary span a smooth surface faithfully approximating the optimized shape.

As illustrated in Figure 2 for 2D and Figure 1 for 3D, our approach consists of two steps. The first optimizes the shape (including its topology) and the distribution of lattice material within the shape. The input includes a design domain and boundary conditions (Figure 1 left and Figure 2a), as well as design specifications such as the target fraction of solid material. The design domain in 3D is represented by a closed triangle surface mesh. This mesh is voxelized, generating finite elements for simulation and optimization. The output is a set of fields, indicating, per element, the occupancy of lattice material, and the orientation and anisotropy of lattice material (Figure 1 second left and Figure 2b). A surface mesh is then reconstructed using Marching Cubes, representing the optimized shape, *i.e.* the interface between elements that are filled with lattice material and that are empty. The shape enclosed by this reconstructed surface mesh (or, the input surface mesh which defines the design domain, in case that the entire design domain is to be filled with lattices) is tetrahedralized. The optimized fields are then interpolated on the vertices of the tetrahedral model. The vertices, including their connectivity and their associated field values, serve as input for the second step, which compiles a globally connected conforming lattice structure composed of struts (Figure 1 second right and Figure 2c). The output lattice structure is encoded by a graph.

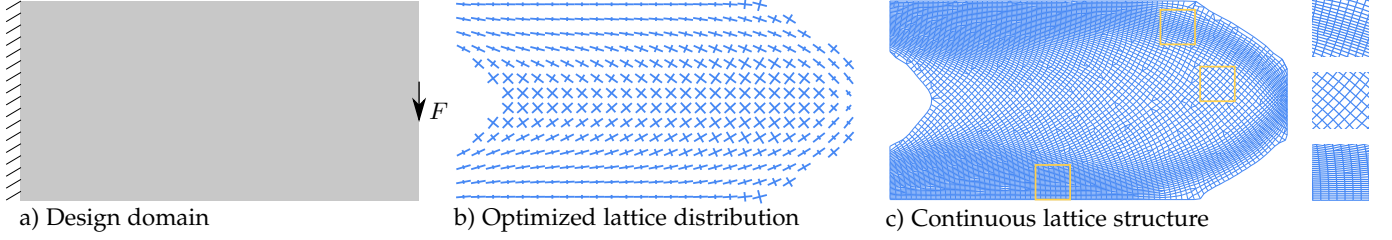


Fig. 2: A 2D example, illustrating the pipeline of our approach. Given the design specification (a), the first step optimizes the distribution of lattice materials (b). The second step extracts a continuous lattice structure corresponding to the optimized lattice configuration (c).

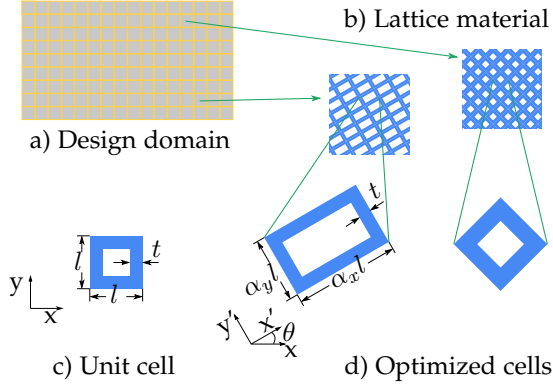


Fig. 3: The design domain (a) is discretized into bilinear quadrilateral elements. Each element is filled with lattice material (b), i.e. a block of periodic cells (d). The cells are adapted by scaling and rotating a unit cell (c).

#### 4 LATTICE OPTIMIZATION

264

The goal of our optimization is to find the optimal distribution of lattice material that maximizes structural stiffness, subject to a number of design constraints. To this end, the design space is discretized into a regular grid of bilinear square elements in 2D or trilinear cubic elements in 3D. As illustrated in Figure 3 for a 2D rectangular design domain, each element is to be filled by repeating a unique, rectangular-shaped cell. The cells are adapted from a unit cell by scaling and rotation. The scaling factors and rotation matrices are to be optimized. The scaling factors for the cell in element  $e$  are denoted by  $\alpha_e$ , and in 2D by  $(\alpha_{e,x}, \alpha_{e,y})$  and in 3D by  $(\alpha_{e,x}, \alpha_{e,y}, \alpha_{e,z})$ . The rotation matrix for element  $e$  is denoted by  $R_e$ .

The unit cell in 2D is a hollowed square with a side length of  $l$  and a thickness of  $t$ , which are specified by the user. In 3D, the cubic unit cell consists of the union of all 12 edges with square cross section of thickness  $t$ . During scaling the side length of cells ( $l$ ) is elongated, while the thickness ( $t$ ) is kept constant. We note that this treatment differs from the standard scaling where the thickness is also scaled. This creates cells with gradation in the fraction of solid material ( $v_e$ ),

$$v_e(\alpha_e) = 1 - \frac{(\alpha_{e,x}l - 2t)(\alpha_{e,y}l - 2t)}{\alpha_{e,x}\alpha_{e,y}l^2}. \quad (1)$$

This gradation allows the optimization to place adapted cells with a smaller fraction of solid material in regions where the stress is relatively small. Furthermore, per axis elongation allows to increase the mechanical anisotropy of

cells. This is beneficial since the stress tensors are typically anisotropic.

Besides a scaling factor per axis and a rotation matrix, each element is assigned a variable  $\varphi_e$ , to indicate whether the element is empty ( $\varphi_e = 0$ ) or filled ( $\varphi_e = 1$ ) with lattice material. The set of elements that are filled with lattice material defines the overall shape of the optimized structure. To allow for gradient-based numerical optimization, the variable  $\varphi_e$  is relaxed to take intermediate values, i.e.  $\varphi_e \in [0, 1]$ . This variable is akin to the density variable in classical density-based topology optimization, which in that context indicates the fraction of *solid* material. In the context of lattice optimization, this variable shall be interpreted as the fraction of *lattice* material. The fraction of solid material per element ( $\rho_e$ ) depends on  $\varphi_e$  and the fraction of solid material within an adapted cell ( $v_e$ ), i.e.

$$\rho_e(\varphi_e, \alpha_e) = \varphi_e v_e(\alpha_e). \quad (2)$$

As the design space is parameterized by the fraction of lattice material ( $\varphi$ ), scaling factor ( $\alpha$ ), and orientation matrix ( $R$ ), the optimization problem is given as

$$\min_{\varphi, \alpha, R} J = \mathbf{F}^T \mathbf{U}(\varphi, \alpha, R) \quad (3a)$$

$$s.t. : \sum_e \rho_e(\varphi_e, \alpha_e) \leq \bar{v}N \quad (3b)$$

$$\varphi_e \in [0.0, 1.0], \forall e \quad (3c)$$

$$\alpha_{e,k} \in [\underline{\alpha}_k, \bar{\alpha}_k], k \in \{x, y, z\}, \forall e. \quad (3d)$$

Here the objective is to minimize the work done by the external force, which is equivalent to minimize compliance (i.e. stiffness maximization).  $\mathbf{F}$  denotes the force vector that is applied to the design domain. The force vector is constant.  $\mathbf{U}$  denotes the displacement vector of the shape when it comes to its static equilibrium under the external force  $\mathbf{F}$ . The first constraint, Eq. 3b, restricts the amount of solid material, where  $\bar{v}$  is the fraction of available solid material, and  $N$  is the number of elements in the design domain. The second constraint, Eq. 3c, sets bounds for the fraction of lattice material ( $\varphi$ ). The third constraint, Eq. 3d, sets bounds for the scaling factors ( $\alpha_x, \alpha_y, \alpha_z$ ). The lower and upper bounds of the scaling factors are user-defined.

The novelty of this formulation is two-fold. First, by optimizing the scaling factors rather than the thickness of hollowed cells, it ensures that all struts in the optimized structure have the same thickness. As discussed in Section 2.2, this eases the control of the 3D printing process. Second, we assign an additional variable  $\varphi$  to indicate the occupation of lattice material. This makes the formulation more general. Prescribing  $\varphi = 1$  leads to optimized lattices

that fill the entire design domain. This is useful as infill for prescribed shapes. Allowing  $\varphi$  to be decided by the optimization enables both the shape and the lattice to evolve simultaneously, achieving a higher stiffness.

#### 4.1 Stiffness Matrix for Lattices

The objective function, Eq. 3a, involves the displacement vector ( $\mathbf{U}$ ), which is related to the external force ( $\mathbf{F}$ ). The unknown  $\mathbf{U}$  is computed by solving the equilibrium equation with finite element analysis,

$$\mathbf{K}(\varphi, \alpha, \mathbf{R})\mathbf{U} = \mathbf{F}. \quad (4)$$

Here the stiffness matrix,  $\mathbf{K}$ , is assembled from per element stiffness matrix,  $\mathbf{K}_e(\varphi_e, \alpha_e, R_e)$ .

In standard finite element analysis of solids [58], the element stiffness matrix  $\mathbf{K}_e$  is computed by integrating over the domain of an element,  $\Omega_e$ ,

$$\mathbf{K}_e = \int_{\Omega_e} B^T D_e B dx, \quad (5)$$

where  $B$  is the element strain-displacement matrix for linear basis functions [58].  $D_e$  represents the fourth order elasticity tensor, computed based on the Young's modulus and Poisson's ratio of the solid material.

For analyzing elements that are filled with lattice material, the elasticity tensor  $D_e$  is not constant but rather depends on design variables  $\alpha_e$  and  $R_e$ . Let us first consider an element that is filled lattice with  $\varphi_e = 1$ . The stiffness matrix for lattices is calculated by

$$\mathbf{K}_e(1, \alpha_e, R_e) = \int_{\Omega_e} B^T D_e(\alpha_e, R_e) B dx, \quad (6)$$

The elasticity tensor of a rotated lattice cell,  $D_e(\alpha_e, R_e)$ , is computed by rotating the elasticity tensor of this cell in its local coordinate system,  $D_e(\alpha_e)$ . In engineering notation,  $D_e$  is represented as a  $3 \times 3$  matrix for 2D problems or a  $6 \times 6$  matrix for 3D. The rotation of tensor is realized by

$$D_e(\alpha_e, R_e) = \bar{R}_e(R_e) D_e(\alpha_e) \bar{R}_e^T(R_e), \quad (7)$$

where the tensor rotation matrix  $\bar{R}$  is given in the Appendix.

The effective elasticity tensor of an elongated cell,  $D_e(\alpha_e)$ , is evaluated by numerical homogenization. We make use of the Matlab code provided in [59] and [60] for homogenization in 2D and 3D, respectively. Given the scaling factors, the domain of the elongated unit cell is discretized by square/cube finite elements with bilinear/trilinear basis functions. To avoid performing homogenization for every  $\alpha_e$  during the optimization process, we precompute  $D_e$  for regularly sampled  $\alpha$  values. In 2D, we fit a surface for every non-zero entry in  $D$  over the 2D domain of  $[\underline{\alpha}_x, \bar{\alpha}_x] \times [\underline{\alpha}_y, \bar{\alpha}_y]$ . In 3D we use trilinear interpolation. The derivative of each non-zero entry in  $D$  with respect to  $\alpha$  is evaluated using the interpolation.

For elements with  $\varphi_e$  between 0 and 1, we use the power law from density-based approaches [34] to interpolate,

$$\mathbf{K}_e(\varphi_e, \alpha_e, R_e) = \varphi_e^p \mathbf{K}_e(1, \alpha_e, R_e), \quad (8)$$

where the parameter  $p$  (typically  $p = 3$ ) is introduced to penalize intermediate values in  $\varphi_e$ , and consequently the optimization steers  $\varphi_e$  towards either 0 or 1.

#### 4.2 Solving

The optimization problem (Eq. 3) is solved in an iterative process, as in [6]. In each iteration the following computational steps are performed, until the maximum change in design variables is smaller than a threshold (or the maximum number of iterations is reached).

First, the equilibrium equation (Eq. 4) is solved, obtaining the displacement vector,  $\mathbf{U}$ . From the element displacement vector ( $\mathbf{U}_e$ ), strain ( $\bar{\epsilon}_e$ ) and stress ( $\bar{\sigma}_e$ ) per element, in engineering notation, are calculated by  $\bar{\epsilon}_e = B\mathbf{U}_e$  and  $\bar{\sigma}_e = D_e(\alpha_e, R_e)\epsilon_e$ , respectively.

Second, design variables  $\varphi$  and  $\alpha$  are updated using a gradient-based solver. We make use of the method of moving asymptotes (MMA) [61]. To avoid checkerboard patterns, the design variables are regularized into  $\tilde{\varphi}$  and  $\tilde{\alpha}$  using the so-called density filter.  $\tilde{\varphi}$  is then projected into  $\bar{\varphi}$  by a (smoothed) Heaviside operation, to approach a 0-1 solution. The filter and Heaviside operator are widely used in density-based approaches, e.g. in [62], [12].

Third, the orientation of each element ( $R_e$ ) is updated based on the associated stress tensor ( $\sigma_e$ ). The stress tensor is symmetric positive-definite. By eigendecomposition we obtain three mutually orthogonal principal stress directions ( $v_1, v_2, v_3$ ). The eigenvectors are ordered by respective eigenvalues in ascending order, i.e.  $\gamma_1 \leq \gamma_2 \leq \gamma_3$ . As shown by Pedersen [3], the optimal orientation of an orthotropic material coincides with the principal stress directions, hence the element is rotated by  $R_e = [v_1^T; v_2^T; v_3^T]$ .

Fourth, the stiffness matrices of lattices,  $K_e$ , are recalculated based on the updated orientation ( $R_e$ ) and regularized variables  $\bar{\varphi}$  and  $\bar{\alpha}$ , according to Section 4.1.

#### 4.3 Example

The output of our optimization is a set of fields defined on the design domain. Figure 4 visualizes these fields for a rectangular domain, which is discretized by a grid of  $80 \times 40$  elements. The unit cell has  $l = 10t$ . The maximum fraction of solid material is 0.15. Figure 4a shows the optimized lattice fraction field. The field contains values very close 0 or 1 (cf. the colorbar). Even with a fraction of solid material as small as 0.15, the lattice covers a large portion of the design space. This is due to the fact that the unit cell has a small fraction of solid material (i.e. 36%, with  $l = 10t$ ). Figure 4b visualizes the orientation of optimized cells. Here the rotated frame is elongated according to the respective scaling factor per axis. For clarity the frames are shown for regularly-spaced samples. On the right, the frame field is visualized for elements which have a fraction of lattice material ( $\varphi_e$ ) that is larger than a threshold (0.5). We note that since the optimized field  $\varphi$  contains values close to 0 or 1, Figure 4c is independent (almost) of the value of the threshold.

### 5 LATTICE COMPILATION

Up to this step, we have equipped with a design domain with a set of fields including fraction of lattice infill, orientation, and scaling, that are optimized for the prescribed external loads (cf Figure 4). Since a region with a low fraction implies that little material is required, we extract

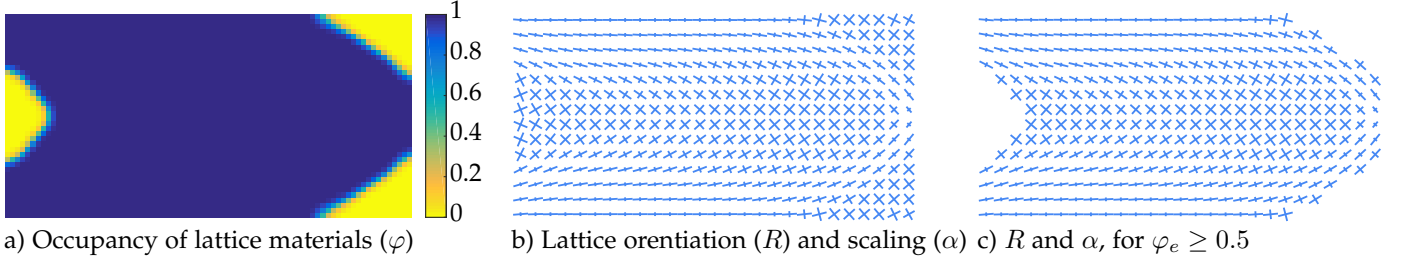


Fig. 4: Visualization of the optimized fields. In (b) and (c) the frame is elongated according to the respective scaling per axis ( $\alpha$ ), and then rotated according to the orientation ( $R$ ).

a sub-area (volume) from the design space by thresholding ( $\geq 0.5$ ) out low infill regions. With the actual shape being extracted, we now focus on generating a lattice structure that conforms to both the boundary of the shape and the directional and scaling fields.

Our problem setting differs from the typical meshing problem in that both of our input and output are quite relaxed from the conditions of being a mesh. For the input, we put no constraints on its geometrical quality (i.e. angles, edge ratios, etc) nor its topological correctness (i.e. permitting non-manifold features, holes, and intersections). This maximizes the scope of the problem but poses a great challenge to the design of a robust solution. For the lattice output, it does not require face (solid) elements, making complex topological operations in most of the meshing methods unnecessary for our purpose. Moreover, considering that it is not a hard requirement for our lattice structure to be all-hex cells for the designed structure to function, we choose the parameterization optimization in [50] that can be easily adapted to handle graphs and propose a simple extraction strategy to generate a lattice structure. The produced lattice structure contains mostly quad (hex)-like connections while allowing certain irregularity to adapt for rapid changes in the directions and scales.

Our method takes a graph with vertices of the optimized shape as the input:  $G = (V, E)$ , where every vertex  $\mathbf{v} \in V$  has a position  $\mathbf{x} \in \mathbb{R}^k$  ( $k$  is 2 for 2D and 3 for 3D), an orientation matrix  $\mathbf{R} \in \mathbb{R}^{k \times k}$  encoding the cross directions and also denoting a local coordinate system, and a scaling vector  $\alpha \in \mathbb{R}^k$  composed of scales for the  $k$  axes of the local coordinate system. Our goal is to extract a lattice structure, which is another graph  $G' = (V', E')$  that (1) reproduces the input direction and anisotropy as much as possible, and (2) has a resolution that can be flexibly controlled by a target edge length  $h$ .

In the following, we first describe the parameterization optimization that incorporates anisotropic orientations, and then present the lattice structure extraction.

## 5.1 Parameterization

Given an orientation field  $\mathbf{O}$  that includes the cross directions for all the vertices, we want to compute a parameterization  $\mathbf{P}$  with the gradient aligned to  $\mathbf{O}$ . Methods that compute a global parameterization with the gradient aligning to the orientation field in a least-square sense (e.g. [63], [64], [43] and [5], [7], [6], [39]), rely on non-linear optimization solvers which are not scalable to large datasets. We instead compute a parameterization for the input graph by representing it with a set of local parameterizations and

minimizing an energy between the local parameterizations of adjacent vertices [57], [50]. The local nature of the parameterization makes it easily parallelizable and scalable to large inputs.

As illustrated in Figure 5a, the local parameterization of a vertex in 2D plane (or 3D volume) can be uniquely determined by its origin  $\mathbf{p}$ , the orientation matrix  $\mathbf{R}$ , and unit lengths  $h \cdot \alpha$ , where  $h$  is the user-defined global target edge length. The unit lengths are fixed through the entire process. Unlike the previous approaches [50], [57] that treat directions as a 4 rotational symmetric field in 2D or a 24 rotational symmetric field in 3D, since the unit length varies for different axis, our coordinate system is mutable only by flipping the signs of each axis. The origin with a random initialization, is the variable we need to optimize.

Given the above setting, the optimization energy of the parameterization  $\mathbf{P}$  is defined as the summation of all the squared differences of local parameterizations for each edge:

$$E(\mathbf{P}) = \sum_{i \in V} \sum_{j \in N(i)} \|\mathbf{p}_i - (\mathbf{M}_{ij} \mathbf{t}_{ij} + \mathbf{p}_j)\|^2, \quad (9)$$

where  $N(i)$  is a set of all the vertices sharing an edge with vertex  $i$ ,  $\mathbf{M}_{ij}$  is an interpolation of  $\mathbf{M}_i$  and  $\mathbf{M}_j$  where  $\mathbf{M} = \mathbf{R}\mathbf{S}$  and  $\mathbf{S}$  is the scaling matrix converted from  $h \cdot \alpha$ , and  $\mathbf{t}_{ij} \in \mathbb{Z}^k$  encodes the integer translations of  $\mathbf{p}_j$ .  $\mathbf{M}_{ij} \mathbf{t}_{ij} + \mathbf{p}_j$  translates  $\mathbf{p}_j$  by integer moves to the nearest position to  $\mathbf{p}_i$ , effectively avoiding the integer jumps between the two local parameterization and only the difference of their fractional parts is measured. The computation of  $\mathbf{M}_{ij}$  requires interpolating the directions and scales separately,

$$\mathbf{M}_{ij} = \text{ortho}(\mathbf{R}_i + \mathbf{R}_j r(\mathbf{R}_i, \mathbf{R}_j)) \cdot \frac{(\mathbf{S}_i + \mathbf{S}_j)}{2}, \quad (10)$$

where  $\text{ortho}$  denotes the orthogonalization of a matrix, and  $r(a, b)$  is the closest matching that gives the smallest difference between two coordinate systems which can be computed efficiently by enumerating all the cases. Note that, there is no scaling involved when computing the matching between orientations, which is similar to the one in [50]. The only difference is that in [50], there are 8 cases to compare for 2D and 48 cases for 3D, while we need to consider 4 and 8 cases in 2D and 3D respectively.

The integer translation between two connecting vertices in the parameterization space,  $\mathbf{t}_{ij}$ , is computed by a rounding operation,

$$\mathbf{t}_{ij} = \text{round}[\mathbf{M}_{ij}^{-1}(\mathbf{p}_i - \mathbf{p}_j)]. \quad (11)$$

By doing so, the energy between the two vertices will be minimized.

521 We minimize  $E(\mathbf{P})$  in a Gauss-Seidel style by iteratively  
 522 visiting every vertex and smoothing the origin of each  
 523 vertex by computing an average of all its neighbors. The  
 524 pseudo code of the optimization is provided in Algorithm 1.

---

**Algorithm 1** Optimize-Parameterizations ( $\mathbf{P}$ )
 

---

```

1: for  $i = 1, \dots, n$  do
2:    $\mathbf{p}'_i \leftarrow \mathbf{p}_i, d \leftarrow 0$ 
3:   for all  $j \in \mathcal{N}(i)$  do
4:      $\mathbf{p}'_i \leftarrow d\mathbf{p}'_i + \mathbf{p}_j + \mathbf{M}_{ij}\mathbf{t}_{ij}$ 
5:      $d \leftarrow d + 1$ 
6:    $\mathbf{p}'_i \leftarrow \mathbf{p}'_i/d$ 
7:   end for
8:    $\mathbf{p}_i \leftarrow \mathbf{p}'_i + \mathbf{M}_i \text{round}[\mathbf{M}_i^{-1}(\mathbf{x}_i - \mathbf{p}'_i)]$ 
9: end for
  
```

---

525

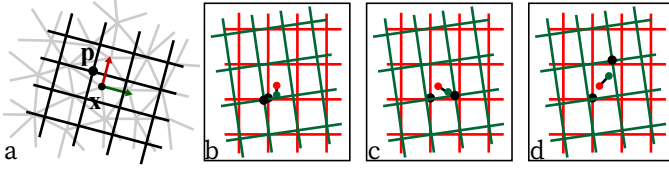


Fig. 5: (a) The local parameterization of a vertex in 2D plane. (b-d) Two local parameterizations of two close vertices in the input graph where they are not necessarily close in the parameterization space.

526 The last step in line 8 rounds each origin of a local  
 527 parameterization  $\mathbf{p}_i$  to the integer position closest to the  
 528 vertex position  $\mathbf{x}_i$ . Consequently, each component of  $\mathbf{t}_{ij}$   
 529 becomes  $-1, 0$ , or  $1$ . For example, as illustrated in Fig.  
 530 5,  $\mathbf{t}_{ij} = (0, 0)$  for Fig. 5b,  $\mathbf{t}_{ij} = (\pm 1, 0)$  or  $(0, \pm 1)$  for  
 531 Fig. 5c, and  $\mathbf{t}_{ij} = (\pm 1, \pm 1)$  for Fig. 5d. We note that this  
 532 approach requires an input graph where the length of edges  
 533 is much smaller than the desired length of the lattice struts,  
 534 otherwise the integer translations after rounding could be  
 535 larger than  $|\pm 1|$ .

536 After the rounding step at line 8 of Algorithm 1, if  
 537 vertex  $i$  is on the input boundary, then  $\mathbf{p}_i$  is projected  
 538 onto the tangent plane of  $i$ . This projection step ensures the  
 539 conformity of the finally extracted lattice structure.

540 To speed up the optimization, similar to [50], we con-  
 541 struct a hierarchical structure of the input graph by halving  
 542 the number of vertices for each level and perform the  
 543 optimization on each level of the hierarchy by 50 iterations  
 544 for 2D and 200 iterations for 3D.

## 545 5.2 Graph Extraction

546 In the input graph  $G$ , each vertex  $\mathbf{v}$  has a smoothed local  
 547 parameterization. The origin  $\mathbf{p}$  of  $\mathbf{v}$  provides a guidance  
 548 for the vertex position in the output graph  $G' = (V', E')$ .  
 549 Besides, the integer translation associated with each edge  
 550  $(\mathbf{v}_i, \mathbf{v}_j)$  of  $G$ ,  $\mathbf{t}_{ij} \in \mathbb{Z}^k (k = 2, 3)$ , categorizes this edge as a  
 551 specific element in  $G'$ , depending on the  $L_0$  norm of  $\mathbf{t}_{ij}$   
 552 which is the number of  $\pm 1$ s in  $\mathbf{t}_{ij}$ . In 3D ( $k = 3$ ), this  
 553 number can be

- 554 • 0 (i.e.  $\mathbf{t}_{ij} = (0, 0, 0)$ ), indicating that the two vertices  
 555 are very close in the parameterization space, and thus  
 556 will be collapsed into a point in  $G'$ ,

- 557 • 1 ( $\mathbf{t}_{ij} = (\pm 1, 0, 0), (0, \pm 1, 0),$  or  $(0, 0, \pm 1)$ ), meaning  
 558 that the edge is parallel to one of the stress directions,  
 559 and thus will be kept in  $G'$ ,
- 560 • 2 ( $\mathbf{t}_{ij} = (\pm 1, \pm 1, 0), (\pm 1, 0, \pm 1),$  or  $(0, \pm 1, \pm 1)$ ) or 3  
 561 ( $\mathbf{t}_{ij} = (\pm 1, \pm 1, \pm 1)$ ), respectively corresponding to a  
 562 rectangular or cuboid diagonal, which deviates from  
 563 the stress directions and thus shall not appear in  $G'$ .

564 For example, black edges and green dashed edges in Fig-  
 565 ure 6 left correspond to  $\|\mathbf{t}_{ij}\|_0 = 1$  and 2, respectively.

566 By utilizing the positional guidance of  $\mathbf{p}$  and the indica-  
 567 tion of  $\mathbf{t}_{ij}$ , the graph extraction is straightforward: collapse  
 568 the edges with  $\|\mathbf{t}_{ij}\|_0 = 0$  (dots in Figure 6 represent  
 569 the averaged positions of collapsed edges), keep the edges  
 570 with  $\|\mathbf{t}_{ij}\|_0 = 1$ , and remove the diagonal edges (i.e.  
 571  $\|\mathbf{t}_{ij}\|_0 = 2$  or 3).

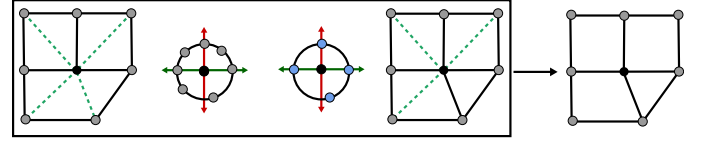


Fig. 6: Left: for a vertex in the graph, the nearest diagonal edges from its rotational directions will be relabelled to be maintained in the final graph if there is no edge representing the corresponding directions. Right: after the relabeling, our final graph is generated by discarding all the diagonal edges.

572 While the above procedure generates a graph with  
 573 mostly right angles, we notice T-junctions in the final graph  
 574 with near flat angles that are suboptimal for the stiffness of  
 575 the lattice structure. Figure 6 left illustrates a vertex with  
 576 T-junction in 2D. This can be attributed to the fact that the  
 577 removal of the diagonal edges is aggressive. The T-junctions  
 578 appear near singularities of the parameterization (similar to  
 579 the positional singularities in [50]) which result in elements  
 580 with non-right angles, for example, triangles and pentagons  
 581 in 2D, and prisms and general polyhedra in 3D.

582 To address this issue, we propose to keep some diagonal  
 583 edges in the final graph. Specifically, right after collapsing  
 584 edges with  $\|\mathbf{t}_{ij}\|_0 = 0$ , we check the configuration of every  
 585 vertex in the graph and identify critical diagonals. As illus-  
 586 trated in Figure 6, for a vertex in black, the process is done  
 587 by first normalizing all of its adjacent edge vectors onto  
 588 a unit circle (sphere in 3D), then computing their nearest  
 589 directions over 4 rotational-symmetric ones in 2D (6 in 3D),  
 590 e.g. red and dark green arrows, and finally relabelling a  
 591 diagonal edge to be an edge with  $\|\mathbf{t}_{ij}\|_0 = 1$  such that each  
 592 of the 4 (6 in 3D) stress directions is represented by an edge  
 593 that is close to the direction (Figure 6 right).

594 In summary, the process to extract the graph  $G'$ , i.e. a  
 595 lattice structure, consists of the following steps.

- 596 1) Categorize the edges in  $G$  based on  $\|\mathbf{t}_{ij}\|_0$ .
- 597 2) Group vertices in  $G$  according to  $\|\mathbf{t}_{ij}\|_0$  such that groups  
 598 are connected by edges with  $\|\mathbf{t}_{ij}\|_0 \neq 0$ . Note that a  
 599 group might contain only a single vertex.
- 600 3) Generate the initial  $G'$ . For each group, a new vertex is  
 601 positioned at the average of the origins of vertices in  $G$ .  
 602 This vertex inherits the edges to new vertices that are  
 603 converted from neighbouring groups.



- 604 4) Categorize the edges in  $G'$  based on  $\|t_{ij}\|_0$ .  
 605 5) Identify and relabel critical diagonals in  $G'$  to avoid T-  
 606 junctions, and remove other diagonal edges.

## 607 6 RESULTS

### 608 6.1 Examples

609 Our method works for both 2D and 3D. Figure 7 shows three  
 610 optimized 2D lattice structures. In (a), the lattice distributes  
 611 across the prescribed curved shape, with spatial variations  
 612 in orientation, porosity, and anisotropy. In (b) and (c), the  
 613 optimized lattices cover a subset of a rectangular design do-  
 614 main, with variations in orientation in (c) and additionally  
 615 variations in porosity and anisotropy in (b). The unit cell in  
 616 2D is specified with  $l = 10t$ ,  $\underline{\alpha} = 1$ , and  $\bar{\alpha} = 4$ .

617 Figure 8 shows 3D lattice structures optimized by our  
 618 method. Our method is also applicable to design lattices  
 619 that spread over a prescribed 3D curved shape, as shown in  
 620 Figure 9. 3D examples are optimized with a unit cell using  
 621  $l = 4t$ ,  $\underline{\alpha} = 1$ , and  $\bar{\alpha} = 2$ . Figure 10 shows fabricated  
 622 bridge and cantilevers. The models are 3D printed with a  
 623 Formlab Form 2 printer which uses stereolithography (SLA).  
 624 The dimension of models and the thickness of struts are  
 625 scaled to comply with the volume and feature size of the  
 626 printer. The printed femur (Figure 11) has a dimension of  
 627  $112.4 \times 77.9 \times 133.1 \text{ mm}^3$ , with a thickness of  $0.5 \text{ mm}$ . The  
 628 chair (Figure 1) is  $110.8 \times 76.6 \times 142.1 \text{ mm}^3$ , with a thickness  
 629 of  $0.6 \text{ mm}$ .

### 630 6.2 Evaluation

#### 631 6.2.1 Design options

632 We evaluate the influence of various design options on  
 633 the resulting lattice structures using the 2D cantilever (   
 634 Section 4.3, Figure 4), with the fraction of solid material  
 635  $\bar{v} = 0.15$ , and bounds for the scaling factors  $\underline{\alpha} = 1$  and  
 636  $\bar{\alpha} = 4$ . The optimized fields and compiled lattice structures  
 637 are shown in Figures 12 and 13, respectively.

638 In the first row of Figure 12, the fraction of lattice is  
 639 fixed,  $\varphi = 1$ . Consequently the lattice distributes across the  
 640 entire rectangular design domain. In (a) the scaling is also  
 641 fixed, while in (b) the optimization of scaling is enabled.  
 642 The enlarged solution space leads a decrease in compliance  
 643 (i.e. improved stiffness), 418.33 (a) vs. 282.62 (b). In (c),  
 644 the scaling factors along individual axes are decoupled,  
 645 resulting in a further decrease in compliance to 239.97.

646 In the second row of Figure 12, the fraction of lattice  
 647 is optimized. Consequently, a shape evolves from the opti-  
 648 mization, corresponding to  $\varphi_e \geq 0.5$ . Similar to the trend of  
 649 compliance in the first row, it decreases from (d), to (e), and  
 650 to (f), along with the increased flexibility in optimization.  
 651 (f) has the smallest compliance among the six cases. It  
 652 decreases from (a) by 44.39%. This study, in agreement with  
 653 similar numerical comparisons for various optimization op-  
 654 tions [7], confirms the significance of adaptive porosity and  
 655 anisotropic features for stiffness maximization [65].

656 As a reference, an axis-aligned uniform lattice struc-  
 657 ture covering the entire domain (i.e. corresponding to the  
 658 initialization of Figure 12) is evaluated. Its compliance is  
 659 852.30, which is more than twice larger than the design in  
 660 Figure 12a, and 3.66 times larger than the design in

Figure 12f. This comparison confirms the importance of  
 aligning anisotropic microstructures with internal stress di-  
 rections for stiffness maximization.

#### 664 6.2.2 Accuracy

665 To evaluate the accuracy of our lattice compilation method,  
 666 we perform a comparison of the compliance predicted by  
 667 homogenization with the compliance of lattice structures  
 668 by a full-resolution finite element analysis. To this end,  
 669 the computational domain of the six lattice structures in  
 670 Figure 13 is discretized by a finite element resolution of  
 671  $4096 \times 2048$ , and analyzed using a geometric multigrid elas-  
 672 ticity solver [66]. The voids among lattices are approximated  
 673 by a weak ersatz material with a (relative) Young's modulus  
 674 of  $10^{-2}$ . The comparison is summarized in Table 1. The  
 675 difference in compliance is between 2.89% and 6.46%. This  
 676 demonstrates that our lattice compilation introduces little  
 677 error to the predicted performance from homogenization-  
 678 based optimization. We note that homogenization theory  
 679 assumes infinite periodicity of the cells, while for fabrication  
 680 the compiled lattice has a finite physical size. This effect has  
 681 been evaluated and reported in e.g. [6], [67]. Furthermore,  
 682 we notice that the compiled lattices exhibit a small number  
 683 of triangles. This also partially explains the discrepancy  
 684 since pure rectangles are assumed in homogenization.

TABLE 1: The difference in compliance predicted by ho-  
 mogenization and a full-resolution analysis, for the lattice  
 structures shown in Fig. 13.

	a	b	c	d	e	f
Homo.	418.33	282.62	239.97	332.81	277.27	232.64
Full res.	444.78	300.15	255.48	323.18	292.66	241.94
Diff.	6.32%	6.20%	6.46%	2.89%	5.55%	4.00%

#### 685 6.2.3 Computational performance

686 Table 2 presents statistics of 3D model complexity and  
 687 computational performance. The experiments were run on a  
 688 standard desktop PC equipped with an Intel Xeon E5-1650  
 689 v3 processor (12 cores) running at 3.5 GHz, 64 GB RAM, and  
 690 an Nvidia GTX1080 graphics card with 8 GB memory. The  
 691 optimization and compilation together take less than 1 hour  
 692 even for complex models such as the chair and femur.

693 The group of columns 2-8 is related to lattice optimiza-  
 694 tion. From the cantilever and bridge examples, it can be  
 695 observed that with increasing design flexibility the compli-  
 696 ance ( $J_{com}$ ) decreases. This agrees with the 2D tests in  
 697 Figure 12. The increased design flexibility is also reflected  
 698 by an increase of time associated with updating stiffness  
 699 matrices, which is counted in  $T_{FEA}$ . The optimization time  
 700 of the gradient-based solver for  $\varphi$  and  $\alpha$ ,  $T_{Opt}$ , increases  
 701 accordingly as well.

702 The resolution of optimized fields is refined by a regular  
 703 subdivision (1 element  $\rightarrow$   $2^3$  elements), followed by tri-  
 704 linear interpolation of the fields. While our lattice compi-  
 705 lation algorithm takes a general graph as the input, in our  
 706 implementation, we use triangle meshes and tetrahedral  
 707 meshes which are purely for the convenience of computing  
 708 vertex normal. This step costs 45~70 seconds (cantilevers,  
 709 Figure 8) to 4 minutes and 26 seconds (chair, Figure 1). The  
 710 refinement generates a large number of vertices (#vertex)

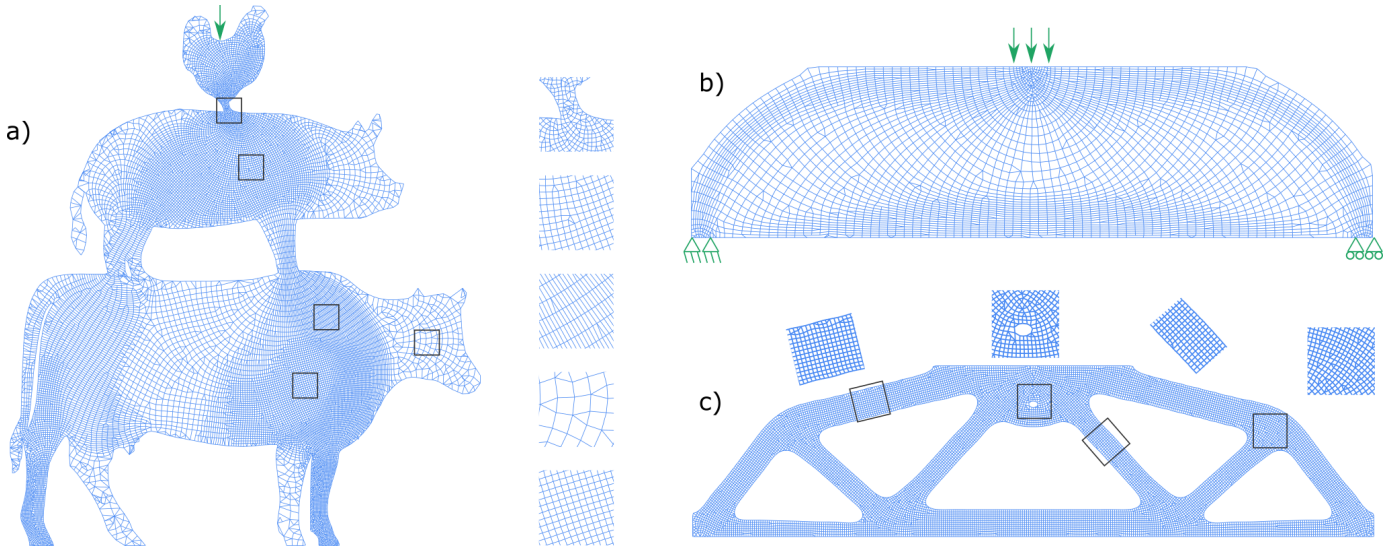


Fig. 7: Optimized 2D lattice structures for a prescribed freeform shape (a) and a rectangular design domain (b and c). The optimized lattice structures possess spatial variations in orientation, porosity, and anisotropy.

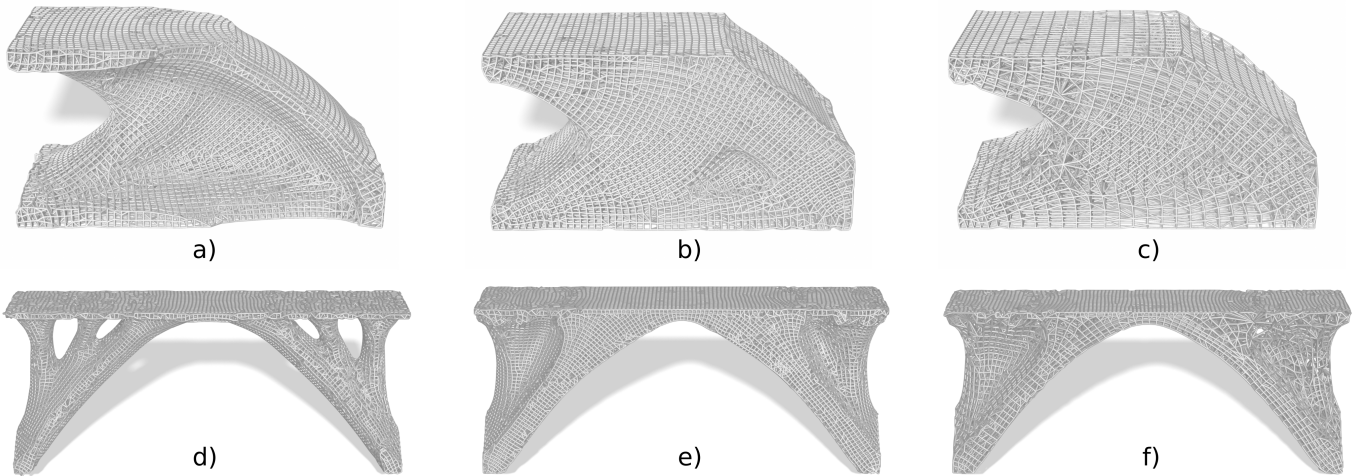


Fig. 8: 3D lattice structures optimized from cuboid design domains, showing spatial variations in orientation, porosity and anisotropy. The design options are: (left) fixed  $\alpha = 1$  with design variables  $R$  and  $\varphi$ , (middle) design variables  $R$ ,  $\varphi$ , and  $\alpha$  with  $\alpha_x = \alpha_y = \alpha_z$ , (right) full flexibility. With the increased design flexibility, the compliance reduces from left to right: 110.84  $\rightarrow$  96.03  $\rightarrow$  85.85 (cantilever), 230.52  $\rightarrow$  177.86  $\rightarrow$  149.96 (bridge).

711 organized as tetrahedral elements (#tet), supplied to the  
 712 lattice compilation. The compiled lattice has as many as  
 713 305k struts, for the femur model. Timings for pre-processing,  
 714 i.e. building data structures ( $T_{pre}$ ), local parameterization  
 715 ( $T_{posy}$ ), and graph extraction ( $T_{extr}$ ) are reported.

716 In the last two rows, the optimized fields are refined  
 717 twice (1 element  $\rightarrow$   $4^3$  elements). This creates highly de-  
 718 tailed lattice structures as shown in Figure 14.

### 719 6.3 Comparison and Discussion

720 **Comparison with solid structures from density-based**  
 721 **topology optimization [34]** A 2D simply supported beam  
 722 is optimized using our method and the classic density-  
 723 based approach – Solid Isotropic Material with Penaliza-  
 724 tion (SIMP). The lattice and solid structure generated by  
 725 our method and SIMP, are shown in Figure 15 a) and b),  
 726 respectively. The physical sizes are  $294.8 \times 74.2 \times 60 \text{ mm}^3$ ,  
 727 and the struts have an in-plane thickness of  $0.8 \text{ mm}$ , which

728 is twice the nozzle size. They were fabricated by a Ultimaker  
 729 S5 printer using flexible TPU (thermoplastic polyurethane)  
 730 material. While the digital models were designed using the  
 731 same fraction of solid material, with 3D printing the lattice  
 732 structure is heavier (52 grams vs. 46 grams) due to the  
 733 delicate tool-path.

734 The load condition of the 3D printed specimen is shown  
 735 in Figure 15c. It is supported at the two ends on the bottom,  
 736 while a downward force is applied on the top middle. To  
 737 avoid out-of-plane buckling of these thin specimens, two  
 738 wooden plates (with open square windows for observation)  
 739 are placed to clamp the specimen (Figure 15d). The clamp-  
 740 ing plates are placed with a gap of  $62 \text{ mm}$ , slightly larger  
 741 than the thickness of the specimen.

742 The force-displacement plots for multiple tests are  
 743 shown in Figure 15e. The forces on the solid structure  
 744 increase more steeply than on the porous structure, meaning  
 745 that the solid structure from SIMP has a higher stiffness.  
 746 However, the forces on the solid structure turn down after

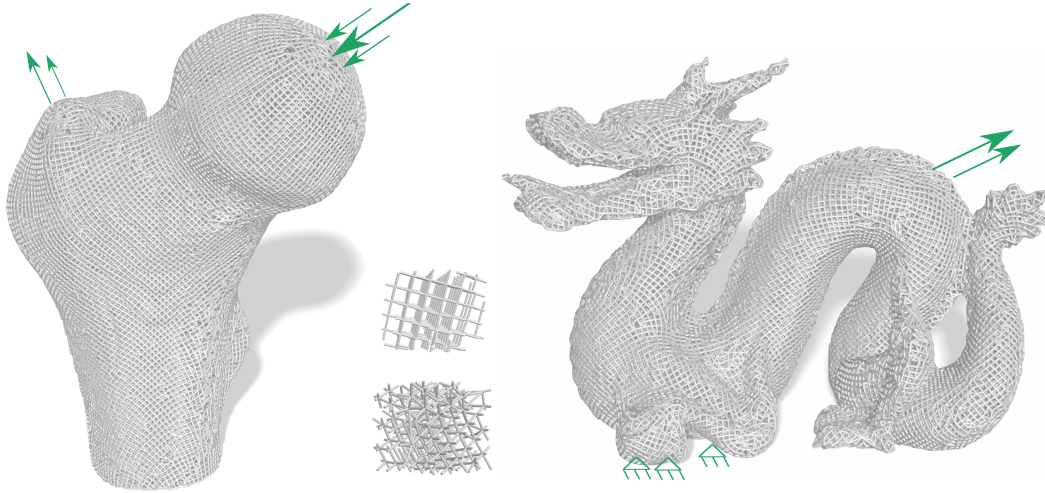


Fig. 9: Optimized 3D lattice structures for prescribed curved shapes. The optimized lattice structures possess spatial variations in orientation. The two samples are taken from inside the femur.

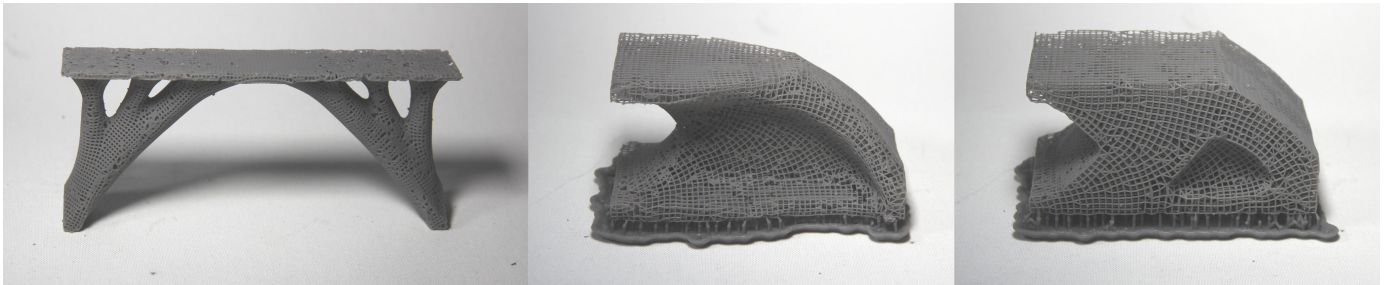


Fig. 10: Optimized lattice structures fabricated by 3D printing.

TABLE 2: Statistics of 3D model complexity and computational performance. The timing is reported in minutes.

Model	Resolution	#Ele.	Vol.	#It.	$J_{com}$	$T_{FEA}$	$T_{Opt}$	#vertex	#tet	#strut	$T_{pre}$	$T_{posy}$	$T_{extr}$	$T_{Total}$
3D cantilever (Fig. 8a)	100 × 50 × 50	250k	0.2	60	110.84	3.11	0.85	0.89m	5.0m	48k	1.80	5.28	0.33	11.36
3D cantilever (Fig. 8b)	100 × 50 × 50	250k	0.2	60	96.03	3.97	1.62	1.65m	9.62m	87k	1.75	9.98	0.70	18.03
3D cantilever (Fig. 8c)	100 × 50 × 50	250k	0.2	60	85.85	5.83	2.65	1.62m	9.41m	25k	1.83	6.50	0.57	17.38
Bridge (Fig. 8d)	200 × 38 × 88	644k	0.1	60	230.52	15.13	1.88	1.18m	6.54m	63k	1.41	7.09	0.47	25.97
Bridge (Fig. 8e)	200 × 38 × 88	644k	0.1	60	177.86	16.76	3.80	2.02m	11.57m	111k	2.84	13.58	1.14	38.12
Bridge (Fig. 8f)	200 × 38 × 88	644k	0.1	60	149.96	21.10	6.29	1.89m	10.77m	35k	2.40	8.29	0.72	38.79
chair (Fig. 1)	140 × 100 × 200	1.8m	0.1	60	193.5	30.92	5.03	3.32m	18.60m	178k	4.15	18.66	1.87	60.63
femur (Fig. 9)	140 × 93 × 182	696k	0.5	6	163.4	0.99	0	5.86m	14.26m	305k	12.36	35.50	5.94	54.79
dragon (Fig. 9)	200 × 90 × 143	461k	0.5	6	99.4	1.12	0	4.09m	23.31m	200k	5.09	24.84	2.88	33.92
3D cantilever (Fig. 14)	100 × 50 × 50	250k	0.2	60	110.84	3.11	0.85	6.65m	38.50m	351k	7.19	33.44	6.25	50.84
Bridge (Fig. 14)	200 × 38 × 88	644k	0.1	60	230.52	15.13	1.88	8.64m	49.63m	462k	12.50	56.56	14.35	100.42

747 they reach a peak of about 62 N. This is due to the (in-  
 748 plane) buckling of the compressed bars. In contrast, the  
 749 lattice structure can support a maximum force that is twice  
 750 larger before it buckles. This is due to the increased effective  
 751 cross-section area of the substructures. This test, in agree-  
 752 ment with previous physical tests on 3D printed isotropic  
 753 infill [68], confirms the significance of lattice structures for  
 754 buckling stability. We note that directly accounting for buck-  
 755 ling stability in topology optimization is more expensive  
 756 than just compliance minimization, due to the less intu-  
 757 itive definition of the buckling mechanism and demanding  
 758 eigenvalue problems [69]. Lattice structures, although not  
 759 directly optimized for maximal buckling load, have a very  
 760 good behaviour against buckling.

**Comparison with bone-like porous structures [12]** Wu  
 et al. proposed a density-based approach to design bone-  
 like porous structures using constraints on local material  
 volume [12]. Figure 16 compares the porous structure and  
 the lattice structure, generated with the same boundary con-  
 ditions (see Fig. 2a) and the same fraction of solid material.  
 The porous structure was optimized with a local volume  
 fraction of 0.36, leading to a total volume fraction of 0.288.  
 We then run lattice optimization with this total volume  
 fraction, with the design options of rotation and scaling.  
 The bone-inspired infill was optimized with a finite element  
 resolution of  $400 \times 200$ , while the lattice was obtained with  
 a simulation resolution of  $80 \times 40$ .

The convergence in compliance is plotted in Figure 16

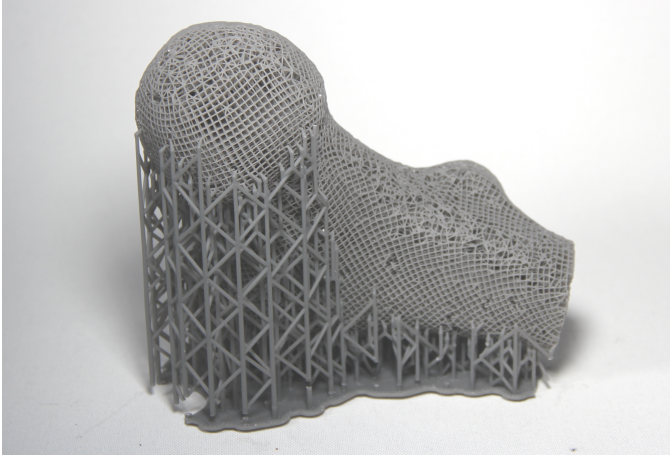


Fig. 11: 3D printed femur with supports.

775 right. The compliance of bone-like infill and conforming  
 776 lattice is 184.64 and 177.29, respectively, meaning that the  
 777 lattice structure is stiffer. Lattice optimization converges  
 778 much faster, and since it runs on a lower resolution, this  
 779 leads to a significant speed up. The optimization of lattice  
 780 took 1 minute and 7 seconds (60 iterations), while the opti-  
 781 mization of bone-like infill cost 40 minutes (1000 iterations).  
 782 Both 2D tests are performed in Matlab.

783 **Discussion of Arora et al. [43]** Arora et al. proposed a  
 784 method to construct a graph with its edges aligned with  
 785 stress directions from simulation of the solid shape [43].  
 786 This approach does not explicitly optimize the porosity nor  
 787 anisotropy. It relates to the option in our method with fixed  
 788  $\varphi$  and  $\alpha$  (cf. Figures 12a and 13a). The result in Figure 12f has  
 789 demonstrated that with optimized porosity and anisotropy,  
 790 the compliance reduces by 44.39%. We note that under  
 791 the option of fixed  $\varphi$  and  $\alpha$ , after aligning the lattice, our  
 792 method re-calculates stress directions and updates the lattice  
 793 orientation. This leads a minor but noticeable decrease in  
 794 compliance than aligning the lattice with stress directions  
 795 from the solid shape (420.58  $\rightarrow$  418.90).

796 Our lattice compilation approach is scalable, for exam-  
 797 ple, the number of struts is more than two orders of mag-  
 798 nitude larger compared with examples shown in [43]. This  
 799 allows to design highly detailed lattice structures. Figure 14  
 800 shows optimized lattice structures with 462k struts (bridge)  
 801 and 351k struts (cantilever).

## 802 7 CONCLUSIONS

803 In this paper we have presented a novel method to design  
 804 conforming lattice structures by homogenization-based  
 805 topology optimization and field-aligned parameterization.  
 806 It can compute not only an optimized lattice structure that  
 807 occupies certain subregions of regular design domains but  
 808 also lattices that spread over prescribed (curved) shapes.  
 809 The optimized lattice structures conform with principal  
 810 stress directions and the boundary of the (optimized) shape.  
 811 Our method is scalable and allows to optimize highly de-  
 812 tailed lattice structures, which can be fabricated by 3D print-  
 813 ing. Numerical analysis on different design options confirms  
 814 the importance of aligning anisotropic lattice with internal  
 815 stress directions and the importance of lattice gradation in  
 816 porosity and anisotropy. The compiled lattice structure, by

a full-resolution finite element analysis, has a compliance 817  
 very close to the compliance predicted by homogenization- 818  
 based optimization. By physical tests we demonstrate that 819  
 the optimized lattice structure can support a buckling load 820  
 twice as large as topology optimized solid structures, at the 821  
 price of a slight decrease in stiffness. Besides quantified 822  
 structural performance, the optimized conforming lattice 823  
 structures look remarkably appealing. 824

**Future work** Our method generates lattice structures par- 825  
 ticularly optimized for mechanical properties. It provides 826  
 options to steer the optimization by configuring the design 827  
 variables, and to adapt the output graph resolution in lattice 828  
 compilation. For designs with lattice spreading across the 829  
 entire design domain, it is found that the generated lattice, 830  
 in certain areas where the stress is small, is less regular, e.g. 831  
 around top right and bottom right corner in Fig. 13 (c), and 832  
 near the boundary at the back of the pig in Fig. 7. This is 833  
 attributed to the fact that principal stress directions, and 834  
 consequently the optimal orientation field, do not coincide 835  
 with the boundary (see the visualization of the orientation 836  
 field in Fig. 12c). A potential solution to this problem is 837  
 to incorporate explicit constraints on the orientation field, 838  
 i.e. enforcing an alignment of the orientation field with the 839  
 prescribed boundary in stress minimal regions. 840

## 841 ACKNOWLEDGEMENTS

The authors gratefully acknowledge the support from the 842  
 LEaDing Fellows Programme at the Delft University of 843  
 Technology, which has received funding from the Euro- 844  
 pean Union's Horizon 2020 research and innovation pro- 845  
 gramme under the Marie Sklodowska-Curie grant agree- 846  
 ment No. 707404. Weiming Wang wishes to thank the Natu- 847  
 ral Science Foundation of China (No. 61702079, U1811463). 848

## 849 APPENDIX

Denoting a  $3 \times 3$  rotation matrix by 850

$$R = \begin{pmatrix} l_1 & l_2 & l_3 \\ m_1 & m_2 & m_3 \\ n_1 & n_2 & n_3 \end{pmatrix}, \quad (12)$$

the  $6 \times 6$  rotation matrix for the elasticity tensor in engineer- 851  
 ing notation is written as 852

$$\bar{R} = \begin{pmatrix} A & B \\ C & D \end{pmatrix}, \quad (13)$$

with 853

$$A = \begin{pmatrix} l_1^2 & m_1^2 & n_1^2 \\ l_2^2 & m_2^2 & n_2^2 \\ l_3^2 & m_3^2 & n_3^2 \end{pmatrix}, \quad (14)$$

$$B = \begin{pmatrix} 2m_1n_1 & 2n_1l_1 & 2l_1m_1 \\ 2m_2n_2 & 2n_2l_2 & 2l_2m_2 \\ 2m_3n_3 & 2n_3l_3 & 2l_3m_3 \end{pmatrix}, \quad (15)$$

$$C = \begin{pmatrix} l_2l_3 & m_2m_3 & n_2n_3 \\ l_3l_1 & m_3m_1 & n_3n_1 \\ l_1l_2 & m_1m_2 & n_1n_2 \end{pmatrix}, \quad (16)$$

and 856

$$D = \begin{pmatrix} m_2n_3 + m_3n_2 & n_2l_3 + n_3l_2 & m_2l_3 + m_3l_2 \\ m_3n_1 + m_1n_3 & n_3l_1 + n_1l_3 & m_3l_1 + m_1l_3 \\ m_1n_2 + m_2n_1 & n_1l_2 + n_2l_1 & m_1l_2 + m_2l_1 \end{pmatrix}. \quad (17)$$

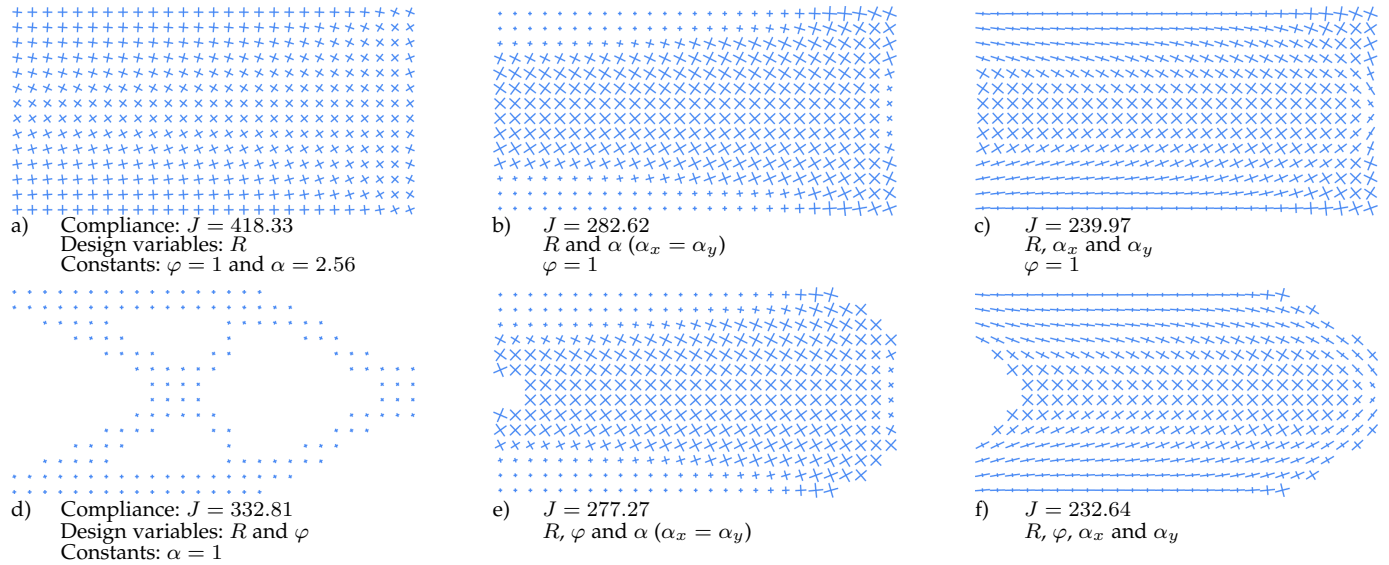


Fig. 12: Visualization of optimized 2D fields corresponding to different design options.

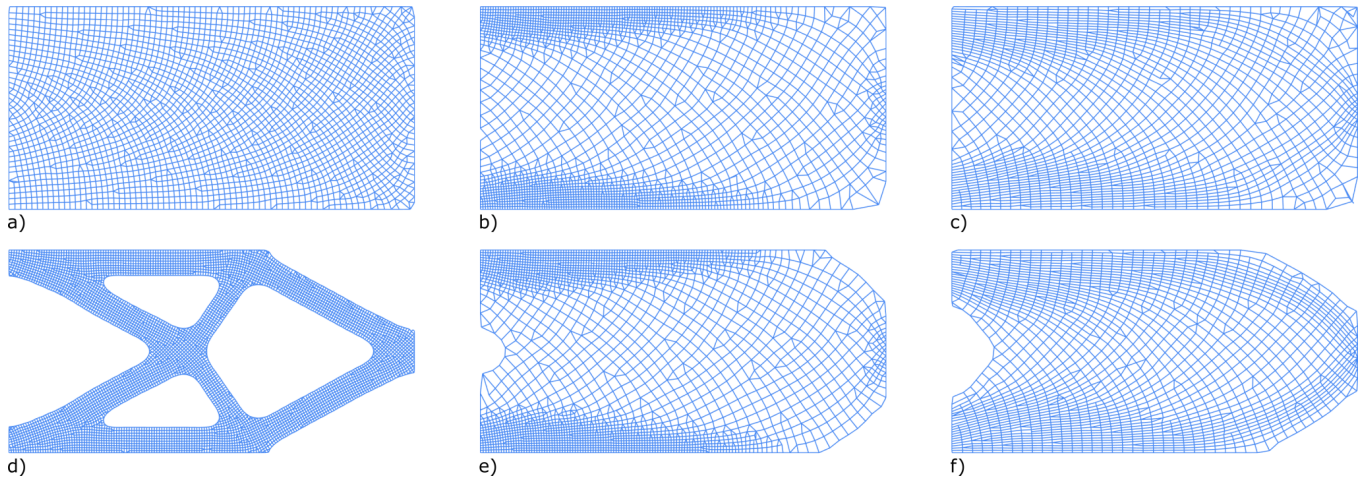


Fig. 13: Compiled lattice structures from the optimized, locally-defined lattice configuration (cf Fig. 12).



Fig. 14: Optimized lattice structures composed of 462k struts (bridge) and 351k struts (cantilever).

**REFERENCES**

857 [1] B. Zhu, M. Skouras, D. Chen, and W. Matusik, "Two-scale  
858 topology optimization with microstructures," *ACM Trans. Graph.*,  
859 vol. 36, no. 5, Jul. 2017.  
860 [2] J. Liu, A. T. Gaynor, S. Chen, Z. Kang, K. Suresh, A. Takezawa,  
861 L. Li, J. Kato, J. Tang, C. C. L. Wang, L. Cheng, X. Liang, and A. C.  
862 To, "Current and future trends in topology optimization for additive  
863 manufacturing," *Structural and Multidisciplinary Optimization*,  
864 vol. 57, no. 6, pp. 2457–2483, Jun 2018.  
865 [3] P. Pedersen, "On optimal orientation of orthotropic materials,"  
866 *Structural optimization*, vol. 1, no. 2, pp. 101–106, Jun 1989.  
867 [4] M. P. Bendsøe and N. Kikuchi, "Generating optimal topologies  
868 in structural design using a homogenization method," *Computer  
869 Methods in Applied Mechanics and Engineering*, vol. 71, no. 2, pp.  
870 197 – 224, 1988.  
871 [5] O. Pantz and K. Trabelsi, "A post-treatment of the homogenization  
872 method for shape optimization," *SIAM Journal on Control and  
873 Optimization*, vol. 47, no. 3, pp. 1380–1398, 2008.  
874

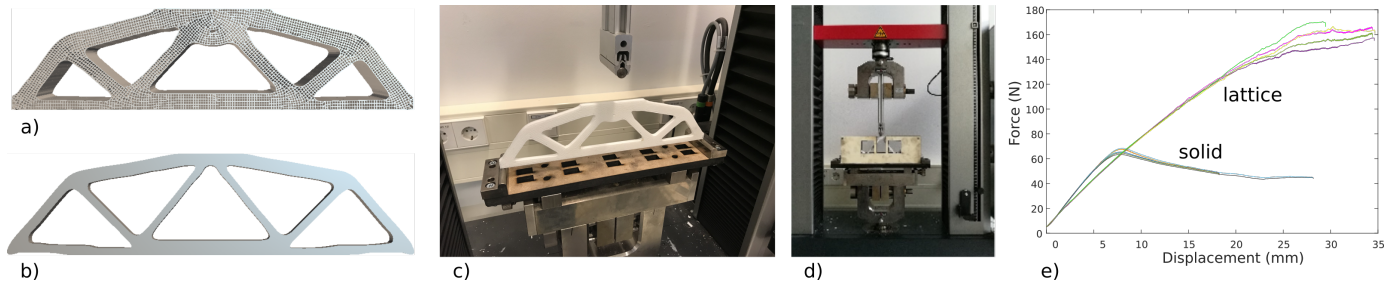


Fig. 15: Physical test comparing an optimized lattice structure (a) with an optimized solid structure (b). (c) and (d) show the experimental setup. From the force-displacement plots for multiple tests (e), it can be observed that, while the lattice structure is slightly less stiff, it supports a compressive force twice larger than the peak force supported by the solid counterpart.

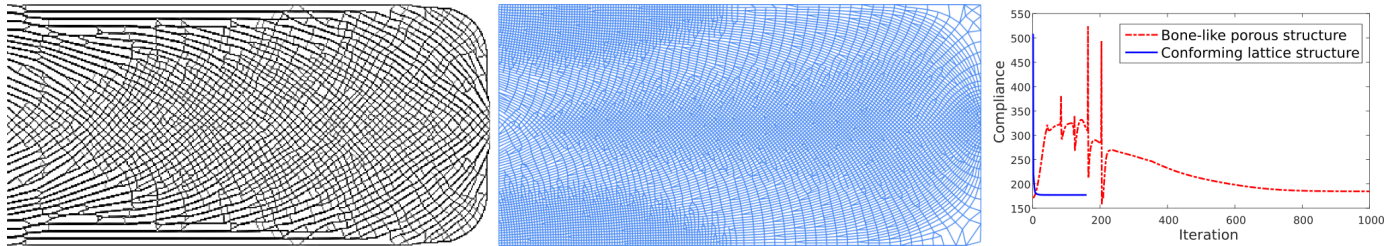
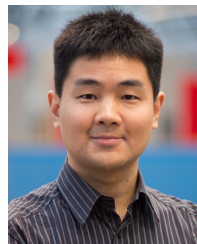


Fig. 16: Left: A bone-like porous structure generated by local volume constraints [12]. Middle: A conforming lattice structure generated by the proposed method. The lattice is stiffer, with a compliance of 177.29, compared to 184.64 of the porous structure. Right: Convergence in compliance for the optimizations.

- 875 [6] J. P. Groen and O. Sigmund, "Homogenization-based topology optimization for high-resolution manufacturable microstructures," *International Journal for Numerical Methods in Engineering*, vol. 113, no. 8, pp. 1148–1163, 2018.
- 876
- 877 [7] G. Allaire, P. Geoffroy-Donders, and O. Pantz, "Topology optimization of modulated and oriented periodic microstructures by the homogenization method," *Computers & Mathematics with Applications*, 2018.
- 878
- 879 [8] M. Attene, M. Livesu, S. Lefebvre, T. Funkhouser, S. Rusinkiewicz, S. Ellero, J. Martínez, and A. H. Bermano, "Design, representations, and processing for additive manufacturing," *Synthesis Lectures on Visual Computing: Computer Graphics, Animation, Computational Photography, and Imaging*, vol. 10, no. 2, pp. 1–146, 2018.
- 880
- 881 [9] W. Wang, T. Y. Wang, Z. Yang, L. Liu, X. Tong, W. Tong, J. Deng, F. Chen, and X. Liu, "Cost-effective printing of 3d objects with skin-frame structures," *ACM Trans. Graph.*, vol. 32, no. 6, pp. 177:1–177:10, Nov. 2013.
- 882
- 883 [10] L. Lu, A. Sharf, H. Zhao, Y. Wei, Q. Fan, X. Chen, Y. Savoye, C. Tu, D. Cohen-Or, and B. Chen, "Build-to-last: Strength to weight 3D printed objects," *ACM Trans. Graph.*, vol. 33, no. 4, pp. 97:1–97:10, Jul. 2014.
- 884
- 885 [11] X. Zhang, Y. Xia, J. Wang, Z. Yang, C. Tu, and W. Wang, "Medial axis tree—an internal supporting structure for 3d printing," *Comput. Aided Geom. Des.*, vol. 35, no. C, pp. 149–162, May 2015.
- 886
- 887 [12] J. Wu, N. Aage, R. Westermann, and O. Sigmund, "Infill optimization for additive manufacturing – approaching bone-like porous structures," *IEEE Transactions on Visualization and Computer Graphics*, vol. 24, no. 2, pp. 1127–1140, February 2018.
- 888
- 889 [13] J. Martínez, J. Dumas, and S. Lefebvre, "Procedural voronoi foams for additive manufacturing," *ACM Trans. Graph.*, vol. 35, no. 4, pp. 44:1–44:12, Jul. 2016.
- 890
- 891 [14] J. Martínez, H. Song, J. Dumas, and S. Lefebvre, "Orthotropic k-nearest foams for additive manufacturing," *ACM Trans. Graph.*, vol. 36, no. 4, pp. 121:1–121:12, Jul. 2017.
- 892
- 893 [15] L. Xia and P. Breitkopf, "Concurrent topology optimization design of material and structure within FE2 nonlinear multiscale analysis framework," *Computer Methods in Applied Mechanics and Engineering*, vol. 278, pp. 524 – 542, 2014.
- 894
- 895 [16] O. Sigmund, N. Aage, and E. Andreassen, "On the (non-)optimality of michell structures," *Structural and Multidisciplinary Optimization*, vol. 54, no. 2, pp. 361–373, Aug 2016.
- 896
- 897 [17] G. Dong, Y. Tang, and Y. F. Zhao, "A survey of modeling of lattice structures fabricated by additive manufacturing," *Journal of Mechanical Design*, vol. 139, no. 10, p. 100906, 2017.
- 898
- 899 [18] F. Tamburrino, S. Graziosi, and M. Bordegoni, "The design process of additive manufactured meso-scale lattice structures: a review," *Journal of Computing and Information Science in Engineering*, vol. 18, no. 4, p. 040801, 2018.
- 900
- 901 [19] H. Wang, Y. Chen, and D. W. Rosen, "A hybrid geometric modeling method for large scale conformal cellular structures," in *ASME 2005 International Design Engineering Technical Conferences and Computers and Information in Engineering Conference*. American Society of Mechanical Engineers, 2005, pp. 421–427.
- 902
- 903 [20] J. Nguyen, S.-I. Park, D. W. Rosen, L. Folgar, and J. Williams, "Conformal lattice structure design and fabrication," in *Solid Freeform Fabrication Symposium, Austin, TX, 2012*, pp. 138–161.
- 904
- 905 [21] A. Michell, "The limits of economy of material in frame-structures," *The London, Edinburgh, and Dublin Philosophical Magazine and Journal of Science*, vol. 8, no. 47, pp. 589–597, 1904.
- 906
- 907 [22] T.-H. Kwok, Y. Li, and Y. Chen, "A structural topology design method based on principal stress line," *Computer-Aided Design*, vol. 80, pp. 19 – 31, 2016.
- 908
- 909 [23] K.-M. M. Tam, C. T. Mueller, J. R. Coleman, and N. W. Fine, "Stress line additive manufacturing (slam) for 2.5-d shells," *Journal of the International Association for Shell and Spatial Structures*, vol. 57, no. 4, pp. 249–259, 2016.
- 910
- 911 [24] M. Kilian, D. Pellis, J. Wallner, and H. Pottmann, "Material-minimizing forms and structures," *ACM Trans. Graphics*, vol. 36, no. 6, p. article 173, 2017.
- 912
- 913 [25] W. Li, A. Zheng, L. You, X. Yang, J. Zhang, and L. Liu, "Rib-reinforced shell structure," *Computer Graphics Forum (Proc. Pacific Graphics)*, vol. 36, no. 7, 2017.
- 914
- 915 [26] J. Smith, J. Hodgins, I. Oppenheim, and A. Witkin, "Creating models of truss structures with optimization," *ACM Trans. Graph.*, vol. 21, no. 3, pp. 295–301, Jul. 2002.
- 916
- 917 [27] T. Zegard and G. H. Paulino, "Grand — ground structure based topology optimization for arbitrary 2d domains using matlab," *Structural and Multidisciplinary Optimization*, vol. 50, no. 5, pp. 861–882, Nov 2014.
- 918
- 919 [28] O. Stava, J. Vanek, B. Benes, N. Carr, and R. Měch, "Stress relief: Improving structural strength of 3d printable objects," *ACM Trans. Graph.*, vol. 31, no. 4, pp. 48:1–48:11, Jul. 2012.
- 920
- 921 [29] Q. Zhou, J. Panetta, and D. Zorin, "Worst-case structural analysis," *ACM Trans. Graph.*, vol. 32, no. 4, pp. 137:1–137:12, Jul. 2013.
- 922
- 923
- 924
- 925
- 926
- 927
- 928
- 929
- 930
- 931
- 932
- 933
- 934
- 935
- 936
- 937
- 938
- 939
- 940
- 941
- 942
- 943
- 944
- 945
- 946
- 947
- 948
- 949
- 950
- 951
- 952
- 953
- 954
- 955
- 956
- 957
- 958

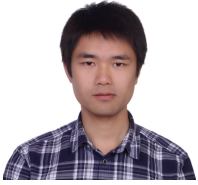
- [30] J. Panetta, A. Rahimian, and D. Zorin, "Worst-case stress relief for microstructures," *ACM Trans. Graph.*, vol. 36, no. 4, pp. 122:1–122:16, Jul. 2017.
- [31] T. Langlois, A. Shamir, D. Dror, W. Matusik, and D. I. W. Levin, "Stochastic structural analysis for context-aware design and fabrication," *ACM Trans. Graph.*, vol. 35, no. 6, pp. 226:1–226:13, Nov. 2016.
- [32] X. Chen, C. Zheng, W. Xu, and K. Zhou, "An asymptotic numerical method for inverse elastic shape design," *ACM Trans. Graph.*, vol. 33, no. 4, pp. 95:1–95:11, Jul. 2014.
- [33] E. Ulu, J. Mccann, and L. B. Kara, "Lightweight structure design under force location uncertainty," *ACM Trans. Graph.*, vol. 36, no. 4, pp. 158:1–158:13, Jul. 2017.
- [34] O. Sigmund, "A 99 line topology optimization code written in matlab," *Structural and multidisciplinary optimization*, vol. 21, no. 2, pp. 120–127, 2001.
- [35] J. Wu, C. Dick, and R. Westermann, "A system for high-resolution topology optimization," *IEEE Transactions on Visualization and Computer Graphics*, vol. 22, no. 3, pp. 1195–1208, March 2016.
- [36] N. Aage, E. Andreassen, B. S. Lazarov, and O. Sigmund, "Giga-voxel computational morphogenesis for structural design," *Nature*, vol. 550, no. 7674, p. 84, 2017.
- [37] H. Liu, Y. Hu, B. Zhu, W. Matusik, and E. Sifakis, "Narrow-band topology optimization on a sparsely populated grid," *ACM Trans. Graph.*, vol. 37, no. 6, pp. 251:1–251:14, Dec. 2018.
- [38] N. Boddeti, Z. Ding, S. Kajijima, K. Maute, and M. L. Dunn, "Simultaneous digital design and additive manufacture of structures and materials," *Scientific reports*, vol. 8, no. 1, p. 15560, 2018.
- [39] P. Geoffroy-Donders, G. Allaire, and O. Pantz, "3-d topology optimization of modulated and oriented periodic microstructures by the homogenization method," " 2018.
- [40] S. Mueller, S. Im, S. Gurevich, A. Teibrich, L. Pfisterer, F. Guimbretière, and P. Baudisch, "Wireprint: 3d printed previews for fast prototyping," in *Proceedings of the 27th Annual ACM Symposium on User Interface Software and Technology*, ser. UIST '14. New York, NY, USA: ACM, 2014, pp. 273–280.
- [41] R. Wu, H. Peng, F. Guimbretière, and S. Marschner, "Printing arbitrary meshes with a 5dof wireframe printer," *ACM Trans. Graph.*, vol. 35, no. 4, pp. 101:1–101:9, Jul. 2016.
- [42] Y. Huang, J. Zhang, X. Hu, G. Song, Z. Liu, L. Yu, and L. Liu, "Framefab: Robotic fabrication of frame shapes," *ACM Trans. Graph.*, vol. 35, no. 6, pp. 224:1–224:11, Nov. 2016.
- [43] R. Arora, A. Jacobson, T. R. Langlois, Y. Huang, C. Mueller, W. Matusik, A. Shamir, K. Singh, and D. I. Levin, "Designing volumetric truss structures," Oct. 2018, arXiv:1810.00706 [cs.GR].
- [44] D. Bommers, B. Lévy, N. Pietroni, E. Puppo, C. Silva, M. Tarini, and D. Zorin, "Quad-mesh generation and processing: A survey," *Comput. Graph. Forum*, vol. 32, no. 6, pp. 51–76, 2013.
- [45] M. Nieser, U. Reitebuch, and K. Polthier, "Cubecover- parameterization of 3d volumes," *CGF*, vol. 30, no. 5, pp. 1397–1406, 2011.
- [46] J. Huang, Y. Tong, H. Wei, and H. Bao, "Boundary aligned smooth 3d cross-frame field," *ACM Trans. Graph.*, vol. 30, no. 6, pp. 143:1–143:8, Dec. 2011.
- [47] Y. Li, Y. Liu, W. Xu, W. Wang, and B. Guo, "All-hex meshing using singularity-restricted field," *ACM Trans. Graph.*, vol. 31, no. 6, pp. 177:1–177:11, Nov. 2012.
- [48] T. Jiang, J. Huang, Y. T. Yuanzhen Wang, and H. Bao, "Frame field singularity correction for automatic hexahedralization," *IEEE TVCG*, vol. 20, no. 8, pp. 1189–1199, Aug. 2014.
- [49] D. Sokolov, N. Ray, L. Untereiner, and B. Lévy, "Hexahedral-dominant meshing," *ACM Trans. Graph.*, vol. 36, no. 4, Jun. 2016.
- [50] X. Gao, W. Jakob, M. Tarini, and D. Panozzo, "Robust hex-dominant mesh generation using field-guided polyhedral agglomeration," *ACM Trans. Graph.*, vol. 36, no. 4, pp. 114:1–114:13, Jul. 2017.
- [51] A. Vaxman, M. Campen, O. Diamanti, D. Panozzo, D. Bommers, K. Hildebrandt, and M. Ben-Chen, "Directional field synthesis, design, and processing," *Computer Graphics Forum*, vol. 35, no. 2, pp. 545–572, 2016.
- [52] N. Ray, D. Sokolov, and B. Lévy, "Practical 3d frame field generation," *ACM Trans. Graph.*, vol. 35, no. 6, pp. 233:1–233:9, Nov. 2016.
- [53] M. Lyon, D. Bommers, and L. Kobbelt, "Hexex: Robust hexahedral mesh extraction," *ACM Trans. Graph.*, vol. 35, no. 4, pp. 123:1–123:11, Jul. 2016.
- [54] J. Solomon, A. Vaxman, and D. Bommers, "Boundary element octahedral fields in volumes," *ACM Trans. Graph.*, vol. 36, no. 3, May 2017.
- [55] H. Liu, P. Zhang, E. Chien, J. Solomon, and D. Bommers, "Singularity-constrained octahedral fields for hexahedral meshing," *ACM Trans. Graph.*, vol. 37, no. 4, pp. 93:1–93:17, Jul. 2018.
- [56] N. Lei, X. Zheng, J. Jiang, Y.-Y. Lin, and D. X. Gu, "Quadrilateral and hexahedral mesh generation based on surface foliation theory," *Computer Methods in Applied Mechanics and Engineering*, vol. 316, pp. 758 – 781, 2017.
- [57] W. Jakob, M. Tarini, D. Panozzo, and O. Sorkine-Hornung, "Instant field-aligned meshes," *ACM Transactions on Graphics (Proceedings of SIGGRAPH ASIA)*, vol. 34, no. 6, Nov. 2015.
- [58] K.-J. Bathe, *Finite element procedures*. Klaus-Jurgen Bathe, 2006.
- [59] E. Andreassen and C. S. Andreassen, "How to determine composite material properties using numerical homogenization," *Computational Materials Science*, vol. 83, pp. 488 – 495, 2014.
- [60] G. Dong, Y. Tang, and Y. F. Zhao, "A 149 line homogenization code for three-dimensional cellular materials written in matlab," *Journal of Engineering Materials and Technology*, vol. 141, no. 1, p. 011005, 2019.
- [61] K. Svanberg, "The method of moving asymptotes a new method for structural optimization," *International Journal for Numerical Methods in Engineering*, vol. 24, no. 2, pp. 359–373, 1987.
- [62] F. Wang, B. S. Lazarov, and O. Sigmund, "On projection methods, convergence and robust formulations in topology optimization," *Structural and Multidisciplinary Optimization*, vol. 43, no. 6, pp. 767–784, Jun 2011.
- [63] D. Bommers, H. Zimmer, and L. Kobbelt, "Mixed-integer quadrangulation," *ACM Trans. Graph.*, vol. 28, no. 3, pp. 77:1–77:10, Jul. 2009.
- [64] T. Jiang, X. Fang, J. Huang, H. Bao, Y. Tong, and M. Desbrun, "Frame field generation through metric customization," *ACM Trans. Graph.*, vol. 34, no. 4, 2015.
- [65] G. Allaire, *Shape optimization by the homogenization method*. Springer Science & Business Media, 2002, vol. 146.
- [66] O. Amir, N. Aage, and B. S. Lazarov, "On multigrid-cg for efficient topology optimization," *Structural and Multidisciplinary Optimization*, vol. 49, no. 5, pp. 815–829, May 2014.
- [67] E. Garner, H. M. Kolken, C. C. Wang, A. A. Zadpoor, and J. Wu, "Compatibility in microstructural optimization for additive manufacturing," *Additive Manufacturing*, vol. 26, pp. 65 – 75, 2019.
- [68] A. Clausen, N. Aage, and O. Sigmund, "Exploiting additive manufacturing infill in topology optimization for improved buckling load," *Engineering*, vol. 2, no. 2, pp. 250 – 257, 2016.
- [69] F. Ferrari and O. Sigmund, "Revisiting topology optimization with buckling constraints," *Structural and Multidisciplinary Optimization*, vol. 59, no. 5, pp. 1401–1415, May 2019.



topology optimization.

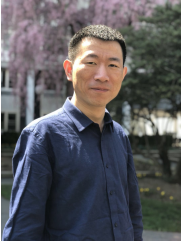
**Dr. Jun Wu** is an assistant professor at the Department of Design Engineering, Delft University of Technology, the Netherlands. Before this, he was a Marie Curie postdoc fellow at the Department of Mechanical Engineering, Technical University of Denmark. He obtained a PhD in Computer Science in 2015 from TU Munich, Germany, and a PhD in Mechanical Engineering in 2012 from Beihang University, Beijing, China. His research is focused on computational design and digital fabrication, with an emphasis on

1095  
1096  
1097  
1098  
1099  
1100  
1101  
1102  
1103  
1104



**Dr. Weiming Wang** is a Marie Curie postdoc fellow at the Department of Design Engineering, Delft University of Technology, the Netherlands, and a lecturer at the School of Mathematical Sciences, Dalian University of Technology, China. He obtained his PhD in the School of Mathematical Sciences in 2016 from Dalian University of Technology, China. His research is focused on digital fabrication and geometry processing.

1105  
1106  
1107  
1108  
1109  
1110  
1111  
1112  
1113  
1114  
1115  
1116



**Dr. Xifeng Gao** is an assistant professor of the Computer Science Department at Florida State University. Dr. Gao was a PostDoc for two years at the Courant Institute of Mathematical Sciences of New York University. He received his Ph.D. degree in 2016 and won the best Ph.D. dissertation award from the Department of Computer Science at the University of Houston. Dr. Gao has wide research interests that are related to geometry, such as Computer Graphics, Visualization, Multimedia Processing, Robotics, and

Digital Fabrication.